coatings

MDPI

Article

Effect of Quenching Cooling Rate on Hydrogen Embrittlement of Precipitation-Hardened Martensitic Stainless Steels

Sicong Shen [1,*], Xingyu Ma [1], Xiaolong Song [2,*], Wenwen Zhao [1] and Yong Shen [3]

[1] College of Materials Science and Engineering, Xi'an Shiyou University, Xi'an 710065, China
[2] State Key Laboratory for Mechanical Behavior of Materials, Xi'an Jiaotong University, Xi'an 710049, China
[3] Institute of Metal Research, Chinese Academy of Sciences, 72 Wenhua Road, Shenyang 110016, China
* Correspondence: scshen@xsyu.edu.cn (S.S.); songxl@mail.xjtu.edu.cn (X.S.)

Abstract: Heat treatment plays a decisive role in the microstructure of metallic materials. The effect of cooling rate changes caused by the quenching medium on the microstructure of steel materials should be clarified. In this study, the effect of the quenching cooling rate on the microstructure of two precipitation-hardened martensitic stainless steels was investigated. The mechanical properties and hydrogen embrittlement susceptibility effected by the changes in the microstructure were also analyzed. A slow tensile test and hydrogen pre-charging were carried out to obtain the hydrogen embrittlement susceptibility parameters of the specimens. The results show that the quenching cooling rate only affects specific microstructures, including the twin structure and misorientation angle. Before hydrogen charging, the mechanical properties of the precipitation-hardened martensitic stainless steels were not affected by changing the quenching cooling rate. After hydrogen charging, the hydrogen embrittlement susceptibility decreased as the quenching cooling rate increased.

Keywords: quenching cooling rate; hydrogen embrittlement; martensitic stainless steels; microstructure

Citation: Shen, S.; Ma, X.; Song, X.; Zhao, W.; Shen, Y. Effect of Quenching Cooling Rate on Hydrogen Embrittlement of Precipitation-Hardened Martensitic Stainless Steels. *Coatings* **2024**, *14*, 572. https://doi.org/10.3390/coatings14050572

Academic Editor: Paolo Castaldo

Received: 19 April 2024
Revised: 2 May 2024
Accepted: 4 May 2024
Published: 6 May 2024

1. Introduction

Precipitation-hardened martensitic stainless steels, such as 17-4 PH, 13-8 PH, and 15-5 PH, which combine good mechanical properties with corrosion resistance, are widely used in industry applications [1–6]. For this kind of steel, the high chromium content ensures excellent corrosion resistance [7], and the outstanding strength derives from two main factors: martensitic hardening during the quenching process and precipitation hardening during aging treatment [8–11]. Heat treatment processing is critical for this steel in practical uses. On the one hand, an appropriate solution treatment temperature can ensure that the precipitation phase element is dissolved in the matrix [12], and research reports [13,14] also prove that the solution treatment temperature is essential to controlling the size of prior austenite grains. On the other hand, the hardness and strength are closely related to the aging treatment temperature [15–17], which has a significant effect on the amount of precipitation in steels.

It is well known that martensitic steels have higher strength and hardness than austenitic steels and ferritic steels. However, the high strength of martensitic stainless steels also brings with it a higher degree of susceptibility to brittle fractures, such as stress corrosion cracking and hydrogen embrittlement. In fact, failures caused by hydrogen embrittlement have been widely studied in the practical application of precipitation-hardened martensitic stainless steels [18–20]. Considering that this kind of steel is designed to be used in corrosive environments, hydrogen may be generated by the electrochemical reaction and be introduced into the materials. So, it is meaningful to enhance the resistance of precipitation-hardened martensitic stainless steels to hydrogen embrittlement.

Heat treatment is widely used to modify the mechanical properties of metal materials for a variety of applications. In this process, as the microstructure changes, the resistance of alloys to hydrogen embrittlement can also be adjusted under proper conditions. Aging

treatment has been studied extensively according to related research reports [21–24], which demonstrate that controlling the aging temperature is effective for enhancing the resistance of reversed austenite to hydrogen embrittlement. It has been reported that solution treatment also has a significant effect on hydrogen embrittlement. As is well known, the prior austenite grain size is related to the solution temperature, and some studies have proven that the grain size can influence the susceptibility to hydrogen embrittlement [25–27].

As an important heat-treatment processing step, quenching has also been investigated in previous studies. Research shows that the microstructure of alloys may change at different quenching cooling rates, which can lead to the enhancement or weakening of the mechanical properties [28–30]. However, few studies have reported on the effect of the quenching cooling rate on brittle fractures caused by hydrogen. Considering the effect of the quenching process on the microstructure, hydrogen embrittlement may be more likely to be influenced by the quenching cooling rate. Hence, this study investigated the effect of the quenching cooling rate on the susceptibility to hydrogen embrittlement of precipitation-hardened martensitic stainless steels. Various quenching mediums were used to obtain different cooling rates. Electrochemical hydrogen charging and slow-strain-rate tensile testing were used to assess the susceptibility to hydrogen embrittlement. Transmission electron microscopy (TEM), X-ray diffraction (XRD), and scanning electron microscopy (SEM) were used to characterize the microstructure and in the fractographic analysis.

2. Materials and Methods

2.1. Material Preparation

The precipitation-hardened martensitic stainless steels 17-4 PH and 13-8 PH were used in this investigation. The chemical compositions of 17-4 PH and 13-8 PH are shown in Table 1. For 17-4 PH, the steel bars ($25 \times 25 \times 62$ mm^3) were heated at 1040 °C for 1 h and then quenched to room temperature. Three quenching mediums, including ambient air, mineral oil, and brine (10% NaCl aqueous solution), were used in the quenching process. In the subsequent aging treatment process, all steel bars were heated at 480 °C for 3 h and then cooled to room temperature in air. For the 13-8 PH steel, the alloy bars were heated at 925 °C for 1 h during the solution treatment stage and quenched using the same three quenching mediums as described above. Then, the steels were subjected to aging treatment (aging at 600 °C for 5 h, cooling in air).

Table 1. Chemical compositions of 17-4 PH and 13-8 PH steels (wt%).

	C	Cr	Ni	Cu	Nb	Mo	Al	Mn	Si
17-4 PH	0.01	16.14	4.07	3.15	0.26	--	--	0.48	0.82
13-8 PH	0.04	12.58	8.26	--	--	2.25	1.07	0.01	0.02

2.2. Microstructure Characterization

After heat-treatment processing, sheet specimens were cut out from the steels with different cooling methods. Then, they were thinned by mechanical polishing using silicon-carbide papers and electrochemically thinned using a twin-jet electropolishing device. A solution consisting of 8 vol% perchloric acid and 92 vol% ethanol was used in the electrochemical thinning process. The microstructures were observed in the ideal thin areas using TEM (equipment model: JEM-200CX, JEOL Ltd., Tokyo, Japan).

Bulk specimens ($12 \times 12 \times 12$ mm^3) were prepared for XRD analysis (equipment model: XRD-7000, Shimadzu X-ray Diffractome, Shimadzu Corporation, Kyoto, Japan). Silicon-carbide papers were used to polish specimens to obtain a smooth surface. The scanning speed was 5 degrees per minute in this test.

2.3. Hydrogen Embrittlement Testing

The hydrogen embrittlement susceptibility of 17-4 PH and 13-8 PH steels was assessed using the electrochemical hydrogen charging method and a slow-strain-rate tensile test.

Cylindrical tensile specimens were machined. As shown in Figure 1, the original diameter, original gauge length, and parallel length of the tensile specimens were 5 mm, 25 mm, and 30 mm, respectively. The surfaces of the specimens were polished using silicon-carbide papers from 240 to 1200 grit.

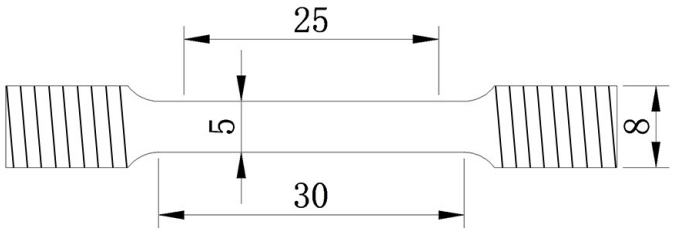

Figure 1. Schematic diagram of a tensile specimen. All dimensions are shown in millimeters (mm).

The polished specimens were hydrogen-charged in a solution consisting of H_2SO_4 (0.5 mol/L) and CH_4N_2S (1 g/L). CH_4N_2S was added in order to prevent the hydrogen from recombining. The screw thread area and transition arc area were covered with paraffin before the specimens were hydrogen-charged. A platinum strip was used as an anode and the tensile specimen was used as the cathode. For the 17-4 PH specimens, the current density was 0.06 mA/cm^2. The current density was 0.12 mA/cm^2 for the 13-8 PH specimens. All specimens were charged for 24 h.

An Instron 1195 mechanical testing system was used in the slow-strain-rate tensile testing. In order to obtain a distinct result between the hydrogen-free specimen and the hydrogen-charged specimen, the nominal tensile strain rate was set to 2×10^{-5}/s.

2.4. Fractographic Analysis

The fractured sections were cut off after tensile testing and observed using SEM (equipment model: SU6600, Hitachi High-Technologies Corporation, Tokyo, Japan). The fracture surface was cleaned using acetone and an ultrasonic cleaning device.

3. Results

3.1. Microstructure

The X-ray diffraction testing results of the 17-4 PH and 13-8 PH steels are shown in Figure 2a,b, respectively. From Figure 2a, it can be seen that, when using the different quenching mediums, the 17-4 PH steels showed only the α phase. This demonstrates that the structure of the 17-4 PH steels had undergone a total transformation from austenite to martensite, and there was no austenite in the air- and brine-quenched steels. For the 13-8 PH steels shown in Figure 2b, the γ phase was observed, which demonstrates that austenite existed in the steels. When comparing the two steels using air and brine quenching, there is no obvious distinction in the relative intensity of the austenite diffraction peak. This indicates that both the air- and brine-quenched steels have the same austenite content. The observed γ-phase diffraction peak was mainly caused by the generation of reversed austenite, which is generated at an over-aged temperature [31,32].

Figures 3 and 4 show the microstructure of the 17-4 PH and 13-8 PH steels using different quenching methods. The feature of a lath martensite structure was observed in both the 17-4 PH and 13-8 PH steels. In Figure 3, the 17-4 PH steels show a martensite structure with a lath width that ranges from 0.5 µm to 0.6 µm. In the case of 13-8 PH steels, the lath width ranges from 0.4 µm to 0.5 µm. The solution treatment temperature was considered to be the main factor that caused the distinction in the martensite lath width. Increasing the solution treatment temperature could result in a greater lath width [33]. By comparing the air-, oil-, and brine-quenched specimens, some twinning structures were observed in the air-quenched specimens for both the 17-4 PH and 13-8 PH steels, which demonstrates that a low cooling rate can result in more twinning structures. Moreover,

precipitates were observed in both the 17-4 PH and 13-8 PH steels, which are exhibited in Figures 3 and 4.

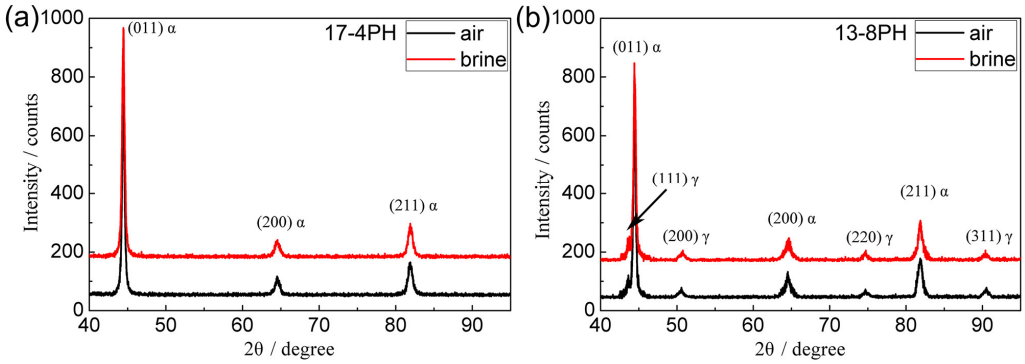

Figure 2. X-ray diffraction patterns of the precipitation- hardened martensitic stainless steels. (**a**) 17-4 PH steels; (**b**) 13-8 PH steels.

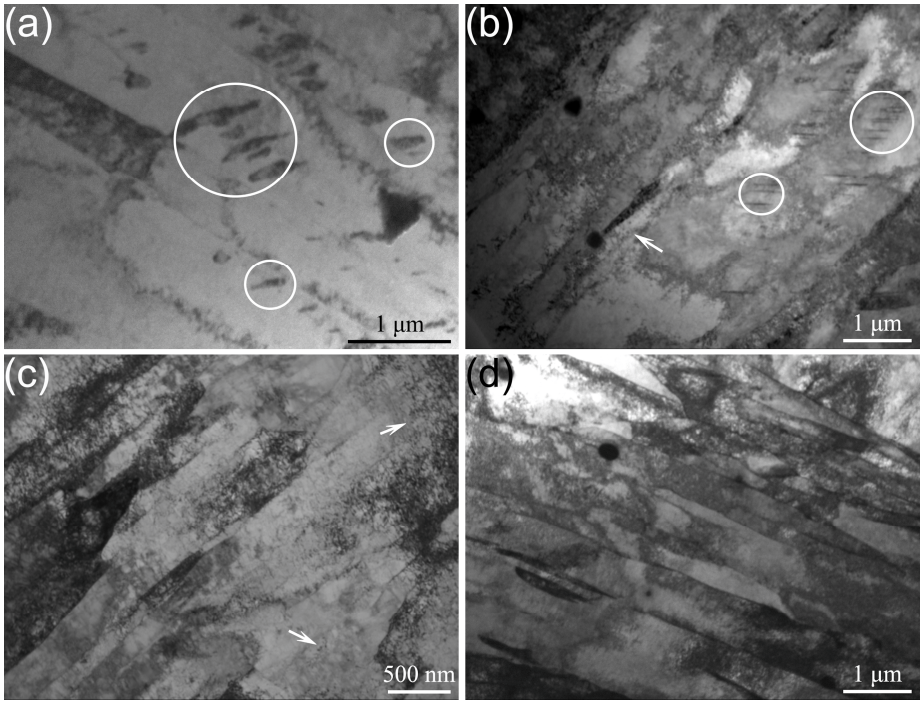

Figure 3. TEM micrographs of the 17-4 PH steels. (**a**,**b**) Air-quenched; (**c**) oil-quenched; (**d**) brine-quenched. The circles show twinning structures, and the arrows show precipitates.

In order to identify the specific structures in the steels, TEM dark-field images were taken in combination with the selected-area diffraction analysis. As shown in Figure 5, copper precipitates can be observed in the dark-field images of all steels using different quenching methods. Some long and thin retained austenite structures can be observed at the lath martensite boundary as shown in Figure 5d. Figure 5c′,d′ show the corresponding selected-area diffraction patterns.

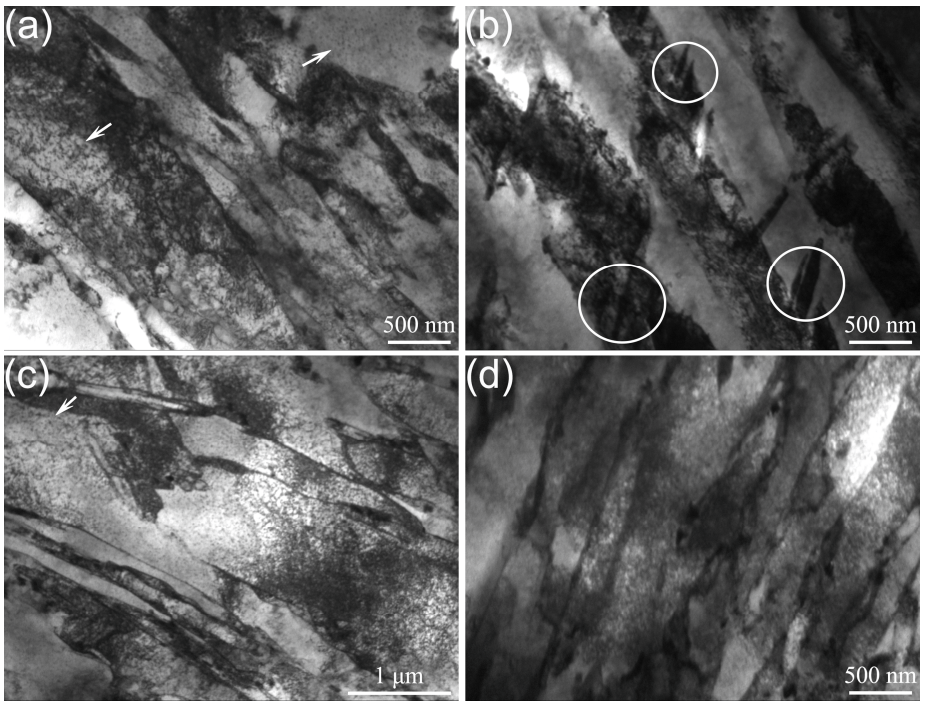

Figure 4. TEM micrographs of the 13-8 PH steels. (**a**,**b**) Air-quenched; (**c**) oil-quenched; (**d**) brine-quenched. The circles show twinning structures, and the arrows show precipitates.

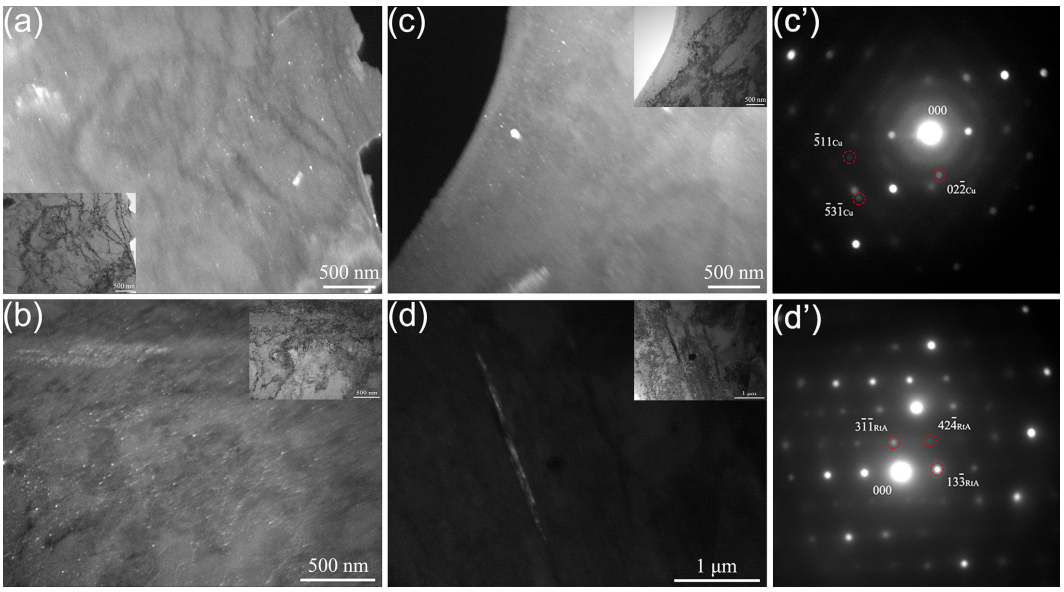

Figure 5. TEM dark-field images of the 17-4 PH steels. (**a**) Air-quenched; (**b**) oil-quenched; (**c**,**d**) brine-quenched; (**c′**) the corresponding selected-area diffraction pattern of (**c**); (**d′**) the corresponding selected-area diffraction pattern of (**d**).

Figure 6 gives the specific microstructures of the 13-8 PH steels. Similarly, NiAl precipitates were observed in the air-, oil-, and brine-quenched steels. Unlike the 17-4 PH steel, reversed austenite was found in the 13-8 PH steel. As shown in Figure 6b, bulk reversed austenite with a size of about 150 × 300 nm^2 was observed in the air-quenched steel. This result is consistent with the X-ray diffraction analysis, in which the austenite phase was found only in the 13-8 PH steel.

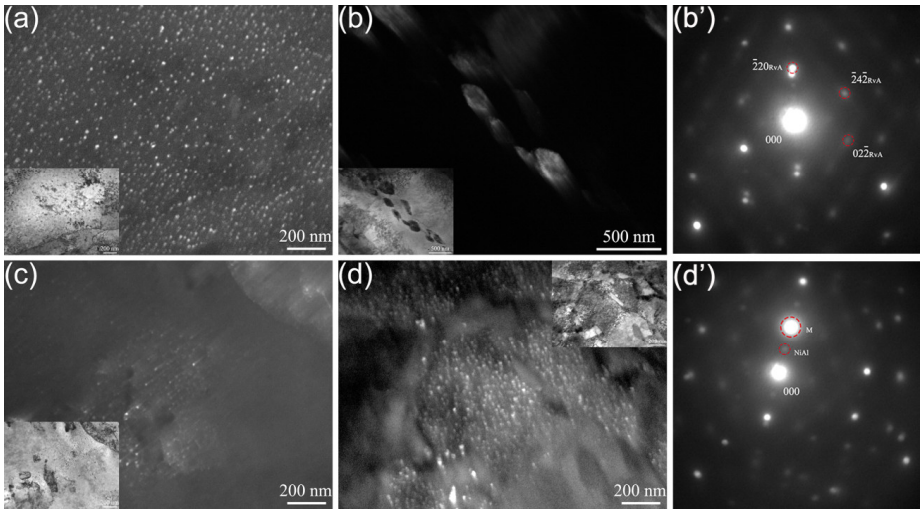

Figure 6. TEM dark-field images of the 13-8 PH steels. (**a**,**b**) Air-quenched; (**c**) oil-quenched; (**d**) brine-quenched; (**b′**) the corresponding selected-area diffraction pattern of (**b**); (**d′**) the corresponding selected-area diffraction pattern of (**d**).

Figures 7 and 8 show the metallographs of the 17-4 PH and 13-8 PH steels. Figure 7a,c show a low- and high-magnification photograph of the air-quenched 17-4 PH steel, respectively. Figure 7b,d show a low- and high-magnification photograph of the brine-quenched specimens. After metallographic corrosion, the prior austenite grain boundary is clearly displayed. It can be seen that there is no obvious difference in the prior austenite grain size of the 17-4 PH steels under the conditions of air quenching and brine quenching. Under the two cooling conditions, the prior austenite grain of the 17-4 PH steel is equiaxed and the grain size ranges from 20 to 25 μm. As a result of metallographic corrosion, lath martensite can be observed in the microstructure of the 17-4 PH steel. A small number of inclusion particles can be seen in Figure 7a,c. The corresponding 13-8 PH steel metallograph is shown in Figure 8, in which (a,c) are air-quenched specimens and (b,d) are brine-quenched specimens. It can be seen that there is little change in the grain size under the two cooling conditions, and the grain size ranges from roughly 25 to 30 μm. Lath martensite can be observed in the 13-8 PH steel with no obvious inclusions. When comparing the metallographs of the different specimens, it can be seen that the microstructure of the two kinds of steel is not very different. The quenching cooling rate has little effect on the grain size and microstructure of the two martensitic stainless steels.

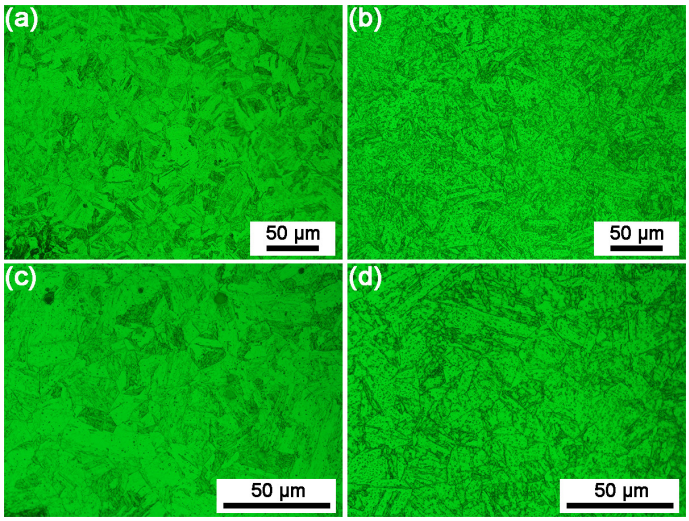

Figure 7. Metallographs of the 17-4 PH steels. (**a**,**c**) Air-quenched; (**b**,**d**) brine-quenched.

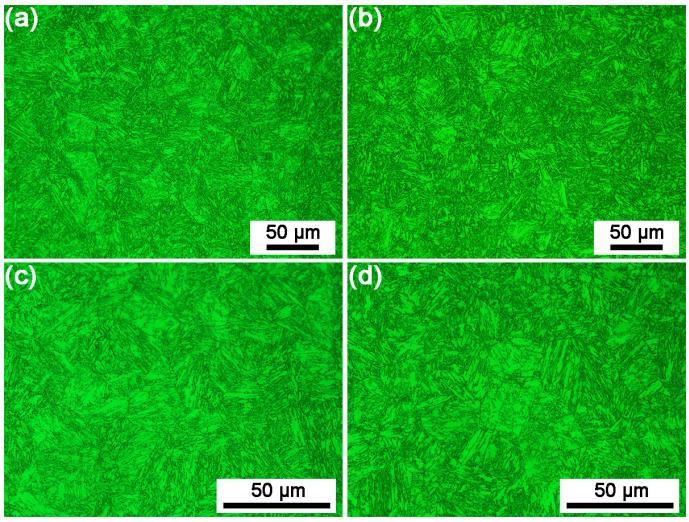

Figure 8. Metallographs of the 13-8 PH steels. (**a**,**c**) Air-quenched; (**b**,**d**) brine-quenched.

3.2. Tensile Properties

Figure 9 shows the tensile test results of the 17-4 PH steel. Figure 9a shows the stress–strain curve of the hydrogen-free (HF, shown with a solid line) and hydrogen-charged (HC, shown with a dashed line) specimens. The air-, oil-, and brine-cooled specimens are represented by black, red, and blue curves, respectively. The calculation of the elongation and reduction in the area for each tensile specimen is given in Figure 9b,c, and the yield strength (YS) and tensile strength (UTS) are shown in Table 2. It can be seen that the 17-4 PH steel without hydrogen has greater strength and plasticity. Under the three cooling conditions, the yield strength and tensile strength are 1265~1293 MPa and 1404~1430 MPa, respectively. The elongation is 13%~15%, and the reduction in the area is roughly 57%. The quenching medium has little effect on the mechanical properties of the 17-4 PH steel without hydrogen. Compared with the HF specimen, the tensile test results of the HC specimen show different situations. After hydrogen charging, the strength of all specimens decreased slightly, but the plasticity decreased significantly (as reflected in the decrease in the elongation and the reduction in the area). Under different quenching cooling rates, different plastic loss amplitudes were obtained. Generally speaking, the lower the cooling rate, the greater the plastic loss. Figure 9d shows the relationship between the hydrogen embrittlement susceptibility index (*HEI*) of the 17-4 PH steel and the cooling rate of the solution treatment. According to the results of the tensile test, the *HEI* was calculated by the relative loss of plasticity, where *HEI-E* and *HEI-A* are related to the elongation and the reduction in area, respectively. The calculation formulas are as follows:

$$HEI - E = \frac{E_F - E_C}{E_F} \quad (1)$$

$$HEI - A = \frac{A_F - A_C}{A_F} \quad (2)$$

where E_F and E_C are the elongation of the HF and HC specimens, respectively, in Formula (1) and A_F and A_C are the reduction in the area of the HF and HC specimens, respectively, in Formula (2). As can be seen from Figure 9d, both the *HEI-E* and *HEI-A* decreased as the solution cooling rate increased.

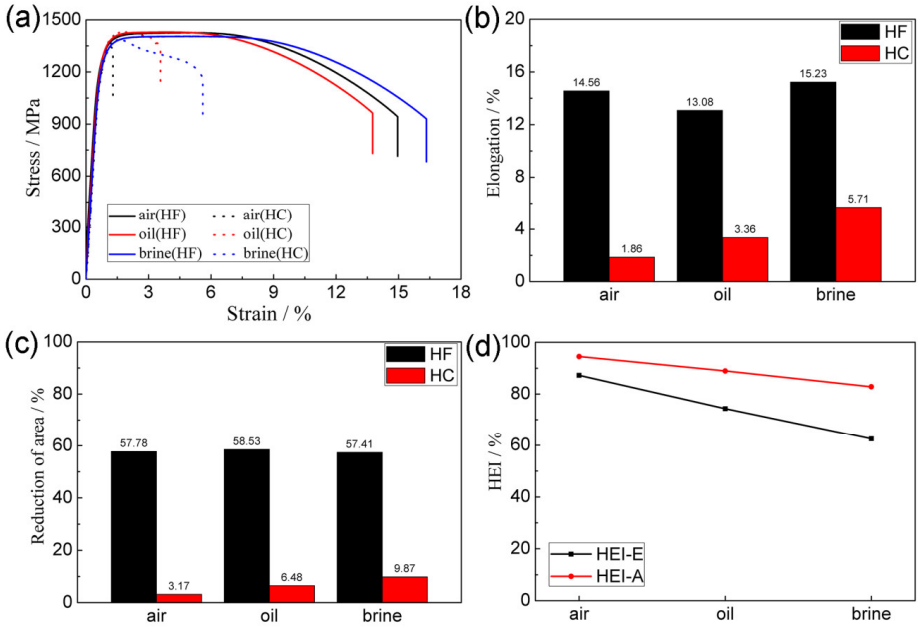

Figure 9. Results of the hydrogen embrittlement test of the 17-4 PH steels. (**a**) Stress–strain curves; (**b**) elongation; (**c**) reduction in area; (**d**) the relationship between the *HEI* and the quenching medium.

Table 2. Mechanical properties of the HF and HC specimens of 17-4PH steel under different cooling conditions.

	Air-Quenched (HF)	Oil-Quenched (HF)	Brine-Quenched (HF)	Air-Quenched (HC)	Oil-Quenched (HC)	Brine-Quenched (HC)
YS (MPa)	1271	1293	1265	1264	1300	1276
UTS (MPa)	1426	1430	1404	1343	1429	1386

Similarly, the tensile test results of the 13-8 PH steel are shown in Figure 10 and Table 3, which display the stress–strain curve, elongation, reduction in area, strength, and related *HEI*. According to the tensile test results, the 13-8 PH steel specimens without hydrogen show little difference in terms of strength and plasticity under the three quenching medium conditions. Compared with the 17-4 PH steel, the 13-8 PH steel has lower strength and greater plasticity. The yield strength and tensile strength are about 1100 MPa and 1190 MPa, respectively. The elongation is 14%~16%, and the reduction in the area is roughly 70%. After hydrogen charging, the plasticity of the 13-8 PH steel also decreased significantly. As displayed in Figure 10d, the *HEI-E* and *HEI-A* of the 13-8 PH steel showed the same variation trend as the 17-4 PH steel (i.e., the *HEI* decreased as the solution cooling rate increased), indicating that the resistance to hydrogen embrittlement can be enhanced by improving the quenching conditions of the solution treatment.

Table 3. Mechanical properties of the HF and HC specimens of 13-8PH steel under different cooling conditions.

	Air-Quenched (HF)	Oil-Quenched (HF)	Brine-Quenched (HF)	Air-Quenched (HC)	Oil-Quenched (HC)	Brine-Quenched (HC)
YS (MPa)	1097	1095	1098	1070	1071	1077
UTS (MPa)	1194	1197	1175	1111	1123	1128

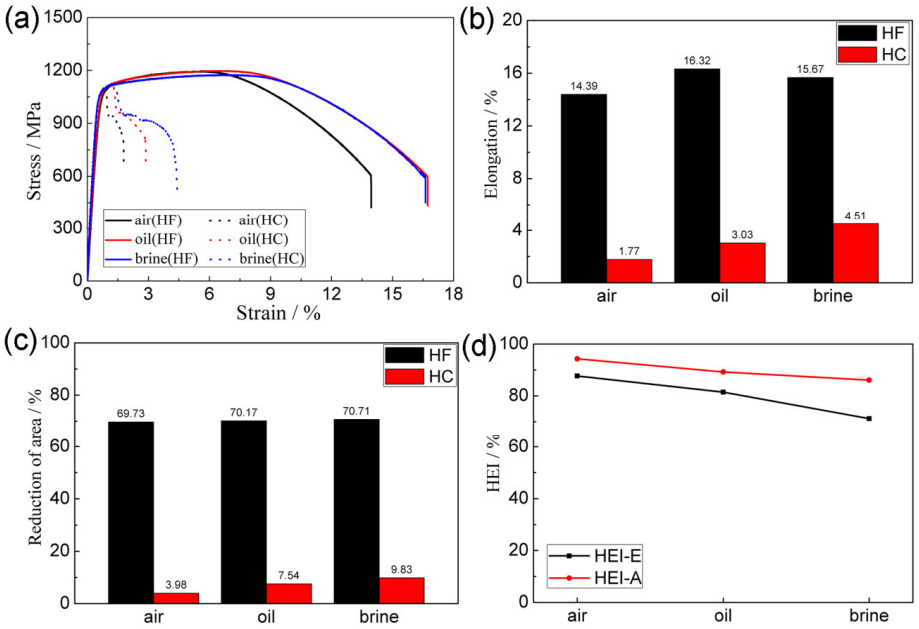

Figure 10. Results of the hydrogen embrittlement test of 13-8 PH steels. (**a**) Stress–strain curves; (**b**) elongation; (**c**) reduction in area; (**d**) the relationship between the *HEI* and the quenching medium.

The transient permeation curves of the specimens are shown in Figure 11, which gives the relationship between the electric current and the permeation time. From the transient permeation curve, the permeability ($J_\infty L$), effective diffusivity (D_{eff}), and apparent solubility (C_{app}) can be calculated. The calculation formulas are as follows:

$$J_\infty L = \frac{I_\infty L}{FA} \tag{3}$$

$$D_{eff} = \frac{L^2}{6t_{0.63}} \tag{4}$$

$$C_{app} = \frac{J_\infty L}{D_{eff}} \tag{5}$$

where I_∞ (A), L (m), A (m^2), $t_{0.63}$ (s), and F are the steady-state current, the specimen's thickness, the exposed surface area of the specimens, the lag time (defined as 0.63 times the steady-state value), and Faraday's constant (96,485 C/mol), respectively.

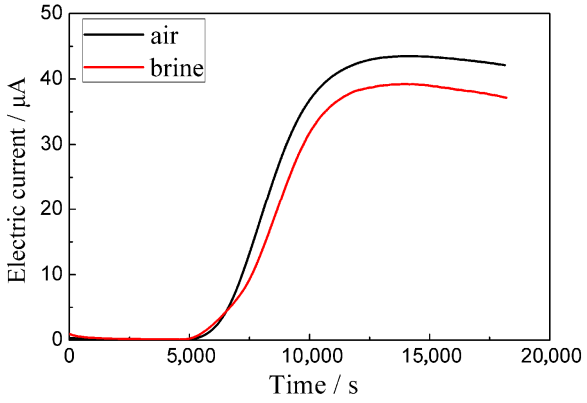

Figure 11. Hydrogen permeation transient curves for 17-4 PH steels under different quenching cooling rates.

The results of the calculations related to the hydrogen penetration test are presented in Table 4. As shown in Table 4, the D_{eff} of hydrogen increased from 1.92×10^{-12} m^2/s to 2.15×10^{-12} m^2/s as the quenching cooling rate increased, while the C_{app} of hydrogen in the alloy showed the opposite trend (it decreased from 375 mol/m^3 to 320 mol/m^3). From the results of the hydrogen penetration test, for the specimens with different quenching cooling rates, the differences in D_{eff} and C_{app} are not obvious, indicating that the quenching cooling rate has less of an influence on the hydrogen diffusion and hydrogen solubility of the martensitic stainless steels.

Table 4. Hydrogen permeation parameters for specimens of 17-4PH steel under different cooling conditions.

	$J_\infty L$ (mol/m s)	D_{eff} (m^2/s)	C_{app} (mol/m^3)
Air-quenched	7.19×10^{-10}	1.92×10^{-12}	375
Brine-quenched	6.88×10^{-10}	2.15×10^{-12}	320

3.3. Fracture Analysis

The SEM images of the fracture in the brine-quenched HF specimens of 17-4 PH steel are given in Figure 12. Figure 12a shows the macroscopic morphology of the fracture, and Figure 12b–d show the microscopic morphology. From the figure, it can be seen that the fracture in the 17-4 PH HF specimen is a typical ductile fracture with obvious necking. The crack initiated in the center region and gradually propagated to the outside. The center region of the fracture has a deep dimple morphology with obvious undulations (as shown in Figure 12b), and the edge region of the fracture has a relatively flat shallow dimple morphology (as shown in Figure 12c,d). From the SEM image, it can be seen that the HF specimen of 17-4 PH steel has good plasticity, which is consistent with its tensile test results.

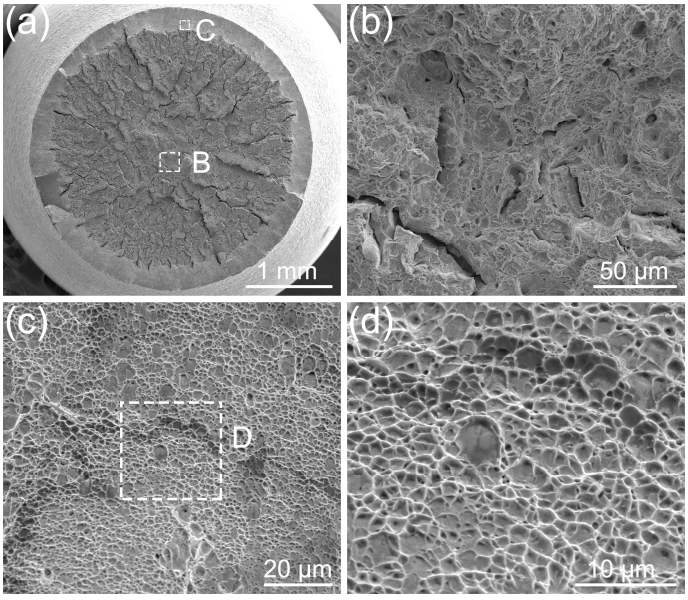

Figure 12. The SEM images of the fracture in the brine-quenched HF specimen of 17-4 PH steel. (**a**) The macroscopic morphology of the fracture; (**b**) high magnification image of region B in (**a**); (**c**) high magnification image of region C in (**a**); (**d**) high magnification image of region D in (**c**).

Figure 13 shows the SEM images of the fracture in the brine-quenched HF specimen of 13-8 PH steel, in which Figure 13a shows the macroscopic morphology of the fracture and Figure 13b–d show the microscopic morphology. The fracture in the 13-8 PH HF specimen is also a ductile fracture. Similarly, the necking is obvious. The crack initiated in the center region, and, finally, an instantaneous fracture occurred at the edge of the fracture. From the

image of the microscopic morphology, it can be seen that the center region of the fracture has a deep dimple morphology (as shown in Figure 13b), while the edge region of the fracture has a shallow dimple morphology (as shown in Figure 13c,d). Based on the fracture morphology, the plasticity of the HF specimen of 13-8 PH steel is also very good. Compared with the 17-4 PH steel, there is no obvious crack propagation region on the fracture surface of the 13-8 PH steel, and the shallow dimple morphology is not obvious in the edge region. The 13-8 PH steel has a higher degree of necking compared with the 17-4 PH steel, which indicates greater plasticity.

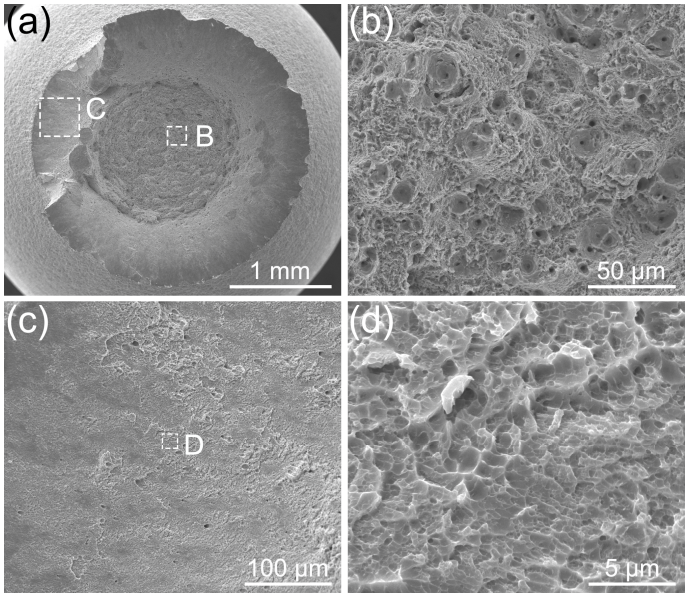

Figure 13. The SEM images of the fracture in the brine-quenched HF specimen of 13-8 PH steel. (**a**) The macroscopic morphology of the fracture; (**b**) high magnification image of region B in (**a**); (**c**) high magnification image of region C in (**a**); (**d**) high magnification image of region D in (**c**).

The SEM images of the fracture in the brine-quenched HC specimen of 17-4 PH steel are given in Figure 14, in which Figure 14a shows the macroscopic morphology and Figure 14b–d show the microscopic morphology. It can be seen from the image of the macroscopic morphology that, after hydrogen charging, the fracture in the 17-4 PH steel changed from a ductile fracture to a brittle fracture. In addition, the fracture does not exhibit the necking feature. The center region of the fracture has a typical quasi-cleavage morphology (as shown in Figure 14b). Compared with a cleavage fracture, the quasi-cleavage fracture shown in the figure is characterized by an obvious tear ridge and a shallow dimple (as shown in Figure 14c), which implies that a certain degree of plasticity has been retained in the 17-4 PH steel after hydrogen charging. The fracture's edge region has a flat and shallow dimple morphology (as shown in Figure 14d), which indicates that the tensile specimen finally fractured in the edge region. The SEM images of the fracture in the HC specimen demonstrate that the plasticity of the 17-4 PH steel deteriorated significantly after hydrogen charging.

Figure 15 shows the SEM images of the fracture in the brine-quenched HC specimen of 13-8 PH steel, in which Figure 15a shows the macroscopic morphology of the fracture and Figure 15b–d show the microscopic morphology. The fracture in the 13-8 PH HC specimen also changed from ductile to brittle and does not exhibit the necking feature. However, compared with the 17-4 PH steel, the brittle fracture characteristics of the 13-8 PH steel are obviously different. The 13-8 PH HC specimen has a shallow dimple morphology at the fracture's center (as shown in Figure 15b) and an along-crystal fracture at the fracture's edge (as shown in Figure 15c). This indicates that, under high-stress conditions, the internal region of 17-4 PH steel is affected by hydrogen earlier, while the external region of

13-8 PH steel is affected by hydrogen earlier. A magnified view of the rectangular region in Figure 15c is shown in Figure 15d, and the clear along-crystal cracks are displayed in the figure. From the figure, it can be roughly judged that the grain size is about 20 to 30 μm, which is consistent with the results shown in the metallograph. Along-crystal fractures and quasi-cleavage fractures are brittle fractures compared with deep dimple fractures, indicating that both martensitic stainless steels become brittle when serviced in a hydrogen-rich environment. Overall, the fracture analysis and tensile testing yielded consistent results.

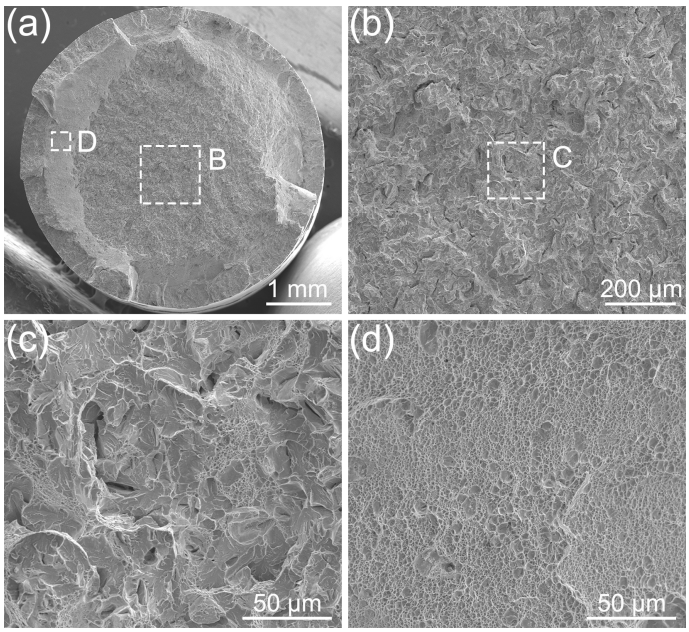

Figure 14. The SEM images of the fracture in the brine-quenched HC specimen of 17-4 PH steel. (**a**) The macroscopic morphology of the fracture; (**b**) high magnification image of region B in (**a**); (**c**) high magnification image of region C in (**b**); (**d**) high magnification image of region D in (**a**).

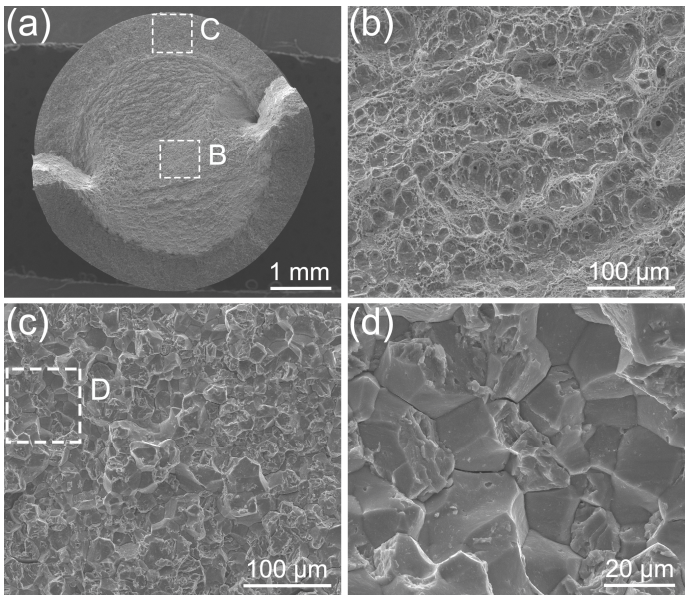

Figure 15. The SEM images of the fracture in the brine-quenched HC specimen of 13-8 PH steel. (**a**) The macroscopic morphology of the fracture; (**b**) high magnification image of region B in (**a**); (**c**) high magnification image of region C in (**a**); (**d**) high magnification image of region D in (**c**).

4. Discussion

4.1. The Effect of the Quenching Cooling Rate on the Microstructure of Precipitation-Hardened Martensitic Stainless Steels

Heat treatment has a significant effect on the microstructure of precipitation-hardened martensitic stainless steels. The grain size, precipitates, reversed austenite, residual austenite, dislocation density, twinning, and misorientation angle will all change as the heat treatment conditions change. The grain size is significantly affected by the solution temperature, i.e., a higher solid solution temperature corresponds to a larger grain size. The size and quantity of precipitates are mainly affected by the aging temperature and aging time. Generally speaking, the higher the aging temperature, the larger the size of the precipitates, and the longer the aging time, the larger the number of precipitates. Reversed austenite generally occurs during the aging process of the alloy and is most significantly affected by the aging temperature. In this study, we only varied the quenching cooling rate after the solution treatment, and the other heat treatment conditions were kept constant. As a result, the microstructure determined by the heat treatment temperature and the heat treatment time was unchanged. In other words, for the 17-4 PH and 13-8 PH martensitic stainless steels, there was no significant difference in the grain size, precipitates, and reversed austenite under the three quenching medium conditions (air, oil, and brine), which is also corroborated by the results of the microstructural analyses, such as the XRD and TEM analyses, and the metallographic analysis.

The quenching cooling rate has a certain effect on the residual austenite, dislocation density, misorientation angle, and twinning structures. In general, the lower the quenching cooling rate, the higher the residual austenite content. On the other hand, the higher the quenching cooling rate, the more difficult it will be for the lattice of atoms to migrate and adjust their position, resulting in the accumulation of dislocations in the vicinity of the grain boundary. This accumulation of dislocations will increase the dislocation density of the alloy. However, based on the results of the XRD and TEM analyses, we did not find a significant amount of residual austenite in the specimens under three different quenching cooling rates, and only a very small amount of residual austenite phase was found in the brine-quenched 17-4 PH specimens. Even under air quenching conditions, the specimens had essentially all transformed from austenite to martensite. This was due to the capacity of precipitation-hardened martensitic steels for martensitic transformation. Based on the results of the microstructural analysis, some twinning structures were found in the air-quenched specimens, while no obvious twinning structures were found in the oil-quenched and brine-quenched specimens. This suggests that a lower quenching cooling rate leads to the generation of twins, probably because a low cooling rate provides time for the growth of twin structures. In addition, the quenching cooling rate has an effect on the misorientation angle. In general, a higher quenching cooling rate will increase the proportion of high-angle grain boundaries. In summary, the quenching cooling rate only has an effect on specific microstructural characteristics. These microstructural changes will have an effect on the materials' mechanical properties and susceptibility to hydrogen embrittlement.

4.2. The Effect of the Quenching Cooling Rate on the Mechanical Properties and Susceptibility to Hydrogen Embrittlement

In this study, all specimens were subjected to tensile tests under three quenching medium conditions. The results show that the HF specimens with different quenching cooling rates did not exhibit any variability in mechanical properties. Specifically, there was no significant difference in strength and plasticity. This is because, for precipitation-hardened martensitic stainless steels, the main structural features affecting the mechanical properties are the grain size, dislocation density, and precipitates. In this study, the temperature and time parameters of the solution and the aging treatments of the same steel had the same values, so there was no significant change in the microstructure of the steel in terms of the grain size, dislocation density, and precipitates. Thus, the specimens with

different quenching cooling rates had the same mechanical properties when subjected to conventional tensile tests in a hydrogen-free environment.

However, after hydrogen charging, the mechanical properties of the specimens with different quenching cooling rates showed some differences, specifically in terms of the plasticity. Subsequently, the hydrogen embrittlement susceptibility obtained from the loss of plasticity showed a corresponding difference. Moreover, the hydrogen embrittlement susceptibility and quenching cooling rate have a certain relationship, that is, as the quenching cooling rate increases, the hydrogen embrittlement susceptibility decreases and the resistance to hydrogen embrittlement increases. These results, in combination with the results of the microstructural analysis, indicate that the difference in the twin structure and misorientation angle is the reason for the change in the hydrogen embrittlement susceptibility.

The twinning structure has a detrimental effect on the hydrogen embrittlement susceptibility of steel materials [34]. It has been shown that, in a hydrogen-rich environment, cracks initiate at the location of twin grain boundaries [35]. Also, due to the high concentration of stress at the tips of the twins, the twins play an important role in crack propagation. In this study, it was found that, for both martensitic stainless steels, the specimen with the air-quenching condition had a more pronounced twin crystal structure. The tensile tests showed that the air-quenched specimen had a higher degree of susceptibility to hydrogen embrittlement, indicating that it was more prone to hydrogen embrittlement. This suggests that a larger number of twinning structures due to a low quenching cooling rate makes the material less resistant to hydrogen embrittlement. On the other hand, the difference in the misorientation angle may also be responsible for the variation in the hydrogen embrittlement susceptibility. The misorientation angle significantly affects the diffusion and trapping of hydrogen atoms in metallic materials. It has been shown that hydrogen has a higher diffusion rate at high-angle grain boundaries and greater segregation at low-angle grain boundaries [36]. The quenching cooling rate has an effect on the misorientation angle, showing that a high cooling rate corresponds to a high proportion of high-angle grain boundaries [37]. It can be inferred that an increase in the cooling rate will lead to higher hydrogen diffusion rates and lower hydrogen concentrations. This is consistent with the results of the hydrogen penetration tests showing that the brine-quenched specimen had a higher hydrogen diffusion rate and a lower hydrogen concentration than the air-quenched specimens. In addition, compared with high-angle grain boundaries, low-angle grain boundaries are more susceptible to corrosion and prone to cracking in a corrosive environment [38]. Therefore, the difference in the misorientation angle caused by the difference in the quenching cooling rate may be another reason for the change in the hydrogen embrittlement susceptibility. Based on the above analysis, for precipitation-hardened martensitic stainless steel, in the case of ensuring that it retains its normal level of plasticity, increasing the quenching cooling rate may be an optional measure to improve the resistance to hydrogen embrittlement.

5. Conclusions

This study investigated the effect of the quenching cooling rate on the microstructure, mechanical properties, and susceptibility to hydrogen embrittlement of precipitation-hardened martensitic stainless steel. Our conclusions can be summarized as follows:

(1) For precipitation-hardened martensitic stainless steels, the quenching cooling rate only affects specific microstructural characteristics. Increasing the quenching cooling rate reduces the number of twin structures and increases the proportion of high-angle grain boundaries;

(2) The mechanical properties of hydrogen-free specimens of precipitation-hardened martensitic stainless steels are not affected by the quenching cooling rate. This is because the quenching cooling rate has little effect on the grain size and precipitates in steels;

(3) The mechanical properties of both 17-4 PH and 13-8 PH are good. After hydrogen charging, both steels exhibited obvious hydrogen embrittlement, which manifested as a substantial loss of plasticity;
(4) The hydrogen embrittlement susceptibility of both 17-4 PH and 13-8 PH decreases as the quenching cooling rate increases. The differences in the twin structure and misorientation angle caused by the quenching cooling rate are the main reasons for the distinct hydrogen embrittlement susceptibility.

Author Contributions: Conceptualization, S.S.; methodology, S.S.; validation, W.Z.; formal analysis, W.Z.; investigation, S.S. and X.M.; writing—original draft preparation, S.S. and X.M.; writing—review and editing, S.S. and Y.S.; supervision, X.S. All authors have read and agreed to the published version of the manuscript.

Funding: This research was funded by the Open Fund of the State Key Laboratory for the Mechanical Behavior of Materials (No. 20222420), the Scientific Research Program Funded by the Shaanxi Provincial Education Department (No. 22JK0507), and the Open Fund of the Shaanxi Key Laboratory of Low Metamorphic Coal Clean Utilization (No. 2021SKL-DBM001).

Institutional Review Board Statement: Not applicable.

Informed Consent Statement: Not applicable.

Data Availability Statement: Data will be made available on request.

Conflicts of Interest: The authors declare no conflicts of interest.

References

1. Couturier, L.; Geuser, F.D.; Descoins, M.; Deschamps, A. Evolution of the microstructure of a 15-5PH martensitic stainless steel during precipitation hardening heat treatment. *Mater. Des.* **2016**, *107*, 416–425. [CrossRef]
2. Bressan, J.D.; Daros, D.P.; Sokolowski, A.; Mesquita, R.A.; Barbosa, C.A. Influence of hardness on the wear resistance of 17-4 PH stainless steel evaluated by the pin-on-disc testing. *J. Mater. Process. Technol.* **2008**, *205*, 353–359. [CrossRef]
3. Shiue, R.K.; Wu, S.K.; Shiue, J.Y. Infrared brazing of Ti–6Al–4V and 17-4 PH stainless steel with (Ni)/Cr barrier layer(s). *Mater. Sci. Eng. A* **2008**, *488*, 186–194. [CrossRef]
4. Sen, D.; Patra, A.K.; Mazumder, S.; Mittra, J.; Dey, G.K.; De, P.K. Carbide precipitates in solution-quenched PH13-8 Mo stainless steel: A small-angle neutron scattering investigation. *Mater. Sci. Eng. A* **2005**, *397*, 370–375. [CrossRef]
5. Pape, J.A.; Neu, R.W. A comparative study of the fretting fatigue behavior of 4340 steel and PH 13-8 Mo stainless steel. *Int. J. Fatigue* **2007**, *29*, 2219–2229. [CrossRef]
6. Shen, S.; Song, X.; Li, Q.; Li, X.; Zhu, R.; Yang, G. Effect of CrxCy–NiCr coating on the hydrogen embrittlement of 17-4 PH stainless steel using the smooth bar tensile test. *J. Mater. Sci.* **2019**, *54*, 7356–7368. [CrossRef]
7. Wang, S.; Quinn, S.; Starink, M.; Wood, R.; Wharton, J. Tribocorrosion damage of a Jethete M152 type stainless steel. *Eng. Fail. Anal.* **2008**, *15*, 903–912. [CrossRef]
8. Hsiao, C.N.; Chiou, C.S.; Yang, J.R. Aging reactions in a 17-4 PH stainless steel. *Mater. Chem. Phys.* **2002**, *74*, 134–142. [CrossRef]
9. Guo, Z.; Sha, W.; Vaumousse, D. Microstructural evolution in a PH13-8 stainless steel after ageing. *Acta Mater.* **2003**, *51*, 101–116. [CrossRef]
10. Ping, D.H.; Ohnuma, M.; Hirakawa, Y.; Kadoya, Y.; Hono, K. Microstructural evolution in 13Cr–8Ni–2.5Mo–2Al martensitic precipitation-hardened stainless steel. *Mater. Sci. Eng. A* **2005**, *394*, 285–295. [CrossRef]
11. Leitner, H.; Schnitzer, R.; Schober, M.; Zinner, S. Precipitate modification in PH13-8 Mo type maraging steel. *Acta Mater.* **2011**, *59*, 5012–5022. [CrossRef]
12. Kakisawa, H.; Minagawa, K.; Kimura, T.; Halada, K. Effect of consolidating temperature on strengthening mechanism in Fe–Cu alloy from rapidly solidified powder. *Mater. Sci. Technol.* **2003**, *19*, 743–748. [CrossRef]
13. Chou, S.L.; Tsai, W.T. Effect of grain size on the hydrogen-assisted cracking in duplex stainless steels. *Mater. Sci. Eng. A* **1999**, *270*, 219–224. [CrossRef]
14. Liu, Y.; Wang, M.; Liu, G. Hydrogen trapping in high strength martensitic steel after austenitized at different temperatures. *Int. J. Hydrogen Energy* **2013**, *38*, 14364–14368. [CrossRef]
15. Tavares, S.S.M.; Silva, F.J.D.; Scandian, C.; Silva, G.F.D.; Abreu, H.F.G.D. Microstructure and intergranular corrosion resistance of UNS S17400 (17-4PH) stainless steel. *Corros. Sci.* **2010**, *52*, 3835–3839. [CrossRef]
16. Chiang, W.C.; Pu, C.C.; Yu, B.L.; Wu, J.K. Hydrogen susceptibility of 17-4 PH stainless steel. *Mater. Lett.* **2003**, *57*, 2485–2488. [CrossRef]
17. Wu, J.H.; Lin, C.K. Effect of strain rate on high-temperature low-cycle fatigue of 17-4 PH stainless steels. *Mater. Sci. Eng. A* **2005**, *390*, 291–298. [CrossRef]

18. Arisoy, C.F.; Başman, G.; Şeşen, M.K. Failure of a 17-4 PH stainless steel sailboat propeller shaft. *Eng. Fail. Anal.* **2003**, *10*, 711–717. [CrossRef]
19. Atxaga, G.; Pelayo, A.; Irisarri, A.M. Failure analysis of a set of stainless steel disc springs. *Eng. Fail. Anal.* **2006**, *13*, 226–234. [CrossRef]
20. Tavares, S.S.M.; Pardal, J.M.; Menezes, L.; Menezes, C.A.B.; D'Ávila, C. Failure analysis of PSV springs of 17-4PH stainless steel. *Eng. Fail. Anal.* **2009**, *16*, 1757–1764. [CrossRef]
21. Ding, Y.S.; Tsay, L.W.; Chiang, M.F.; Chen, C. Gaseous hydrogen embrittlement of PH 13-8 Mo steel. *J. Nucl. Mater.* **2009**, *385*, 538–544. [CrossRef]
22. Tsay, L.W.; Chi, M.Y.; Chen, H.R.; Chen, C. Investigation of hydrogen sulfide stress corrosion cracking of PH 13-8 Mo stainless steel. *Mater. Sci. Eng. A* **2006**, *416*, 155–160. [CrossRef]
23. Li, X.; Zhang, J.; Chen, J.; Shen, S.; Yang, G.; Wang, T.; Song, X. Effect of aging treatment on Hydrogen embrittlement of PH 13-8 Mo martensite stainless steel. *Mater. Sci. Eng. A* **2015**, *651*, 474–485. [CrossRef]
24. Tsay, L.W.; Chi, M.Y.; Wu, Y.F.; Wu, J.K.; Lin, D.Y. Hydrogen embrittlement susceptibility and permeability of two ultra-high strength steels. *Corros. Sci.* **2006**, *48*, 1926–1938. [CrossRef]
25. Chen, S.; Zhao, M.; Rong, L. Effect of grain size on the hydrogen embrittlement sensitivity of a precipitation strengthened Fe–Ni based alloy. *Mater. Sci. Eng. A* **2014**, *594*, 98–102. [CrossRef]
26. Shen, S.; Li, X.; Zhang, P.; Nan, Y.; Yang, G.; Song, X. Effect of solution-treated temperature on hydrogen embrittlement of 17-4 PH stainless steel. *Mater. Sci. Eng. A* **2017**, *703*, 413–421. [CrossRef]
27. Fuchigami, H.; Minami, H.; Nagumo, M. Effect of grain size on the susceptibility of martensitic steel to hydrogen-related failure. *Philos. Mag. Lett.* **2006**, *86*, 21–29. [CrossRef]
28. Zhang, Z.; Wang, W.; Fu, H.; Xie, J. Effect of quench cooling rate on residual stress, microstructure and mechanical property of an Fe–6.5Si alloy. *Mater. Sci. Eng. A* **2011**, *530*, 519–524. [CrossRef]
29. Ammar, H.R.; Moreau, C.; Samuel, A.M.; Samuel, F.H.; Doty, H.W. Influences of alloying elements, solution treatment time and quenching media on quality indices of 413-type Al–Si casting alloys. *Mater. Sci. Eng. A* **2008**, *489*, 426–438. [CrossRef]
30. Nishibata, T.; Kojima, N. Effect of quenching rate on hardness and microstructure of hot-stamped steel. *J. Alloys Compd.* **2013**, *577*, S549–S554. [CrossRef]
31. Bilmes, P.D.; Solari, M.; Llorente, C.L. Characteristics and effects of austenite resulting from tempering of 13Cr–NiMo martensitic steel weld metals. *Mater. Charact.* **2001**, *46*, 285–296. [CrossRef]
32. Schnitzer, R.; Radis, R.; Nöhrer, M.; Schober, M.; Hochfellner, R.; Zinner, S.; Povoden-Karadeniz, E.; Kozeschnik, E.; Leitner, H. Reverted austenite in PH 13-8 Mo maraging steels. *Mater. Chem. Phys.* **2010**, *122*, 138–145. [CrossRef]
33. Maddi, L.; Ballal, A.R.; Peshwe, D.R.; Paretkar, R.K.; Laha, K.; Mathew, M.D. Effect of tempering temperature on the stress rupture properties of Grade 92 steel. *Mater. Sci. Eng. A* **2015**, *639*, 431–438. [CrossRef]
34. Zan, N.; Ding, H.; Guo, X.F.; Tang, Z.Y.; Bleck, W. Effects of grain size on hydrogen embrittlement ina Fe-22Mn-0.6C TWIP steel. *Int. J. Hydrogen Energy* **2015**, *40*, 10687–10696. [CrossRef]
35. Koyama, M.; Akiyama, E.; Tsuzaki, K.; Raabe, D. Hydrogen-assisted failure in a twinning-induced plasticity steel studied under in situ hydrogen charging by electron channeling contrast imaging. *Acta Mater.* **2013**, *61*, 4607–4618. [CrossRef]
36. Oudriss, A.; Creus, J.; Bouhattate, J.; Conforto, E.; Berziou, C.; Savall, C.; Feaugas, X. Grain size and grain-boundary effects on diffusion and trapping of hydrogen in pure nickel. *Acta Mater.* **2012**, *60*, 6814–6828. [CrossRef]
37. Deng, W.; Gao, X.; Qin, X.; Gao, X.; Zhao, D.; Du, L. Effect of cooling rate on microstructure of deformed and undeformed X80 pipeline steels. *Acta Metal. Sin.* **2010**, *46*, 959–966. [CrossRef]
38. Ma, Z.; Liu, J.; Liu, S.; Zhang, Y.; Deng, Y. Quench-induced contributions of high angle grain boundary and low angle grain boundary to exfoliation corrosion propagation in an AlZnMgCu alloy. *J. Mater. Res. Technol.* **2021**, *15*, 6866–6870. [CrossRef]